Ductile rupture of prestrained X100 pipeline steel sheets

Jacques Besson, Yasuhiro Shinohara, Thilo F. Morgeneyer, Yazid Madi

Ductile rupture of prestrained X100 pipeline steel sheets

Jacques Besson[1, a], Yasuhiro Shinohara,[1, b], Thilo F. Morgeneyer[1, c], Yazid Madi[1, 2, d]

[1] Centre des Matériaux, Mines Paristech, CNRS UMR 7633
BP 87, 91003 Evry Cedex, France
[2] Ermess, EPF - Ecole d'Ingénieurs, 3 bis, rue Lakanal 92330 Sceaux, France
[a] jacques.besson@ensmp.fr, [b] yasuhiro.shinohara@mat.ensmp.fr, [c] thilo.morgeneyer@ensmp.fr,
[d] yazid.madi@mat.ensmp.fr

Keywords: Prestrain, X100 steel, ductile rupture, anisotropy, toughness

Abstract. The mechanical and damage behavior of a X100 steel after prestrain is studied in this work. Experimental results show both a plastic and rupture anisotropy: the T direction exhibits a higher ultimate stress but the lowest ductility and toughness. Prestrain reduces ductility and crack growth resistance. A model able to represent the plastic and damage behaviour of the material before and after prestrain is proposed. The model incorporates plastic anisotropy, kinematic hardening, void growth of the primary cavities, nucleation of secondary voids on carbides. Using the model after implementation in a FE software, allows to reproduce experimental trends.

Introduction

Large size pipeline elements are produced by forming and welding steel plates following the UOE process. Forming induces prestraining which both hardens and damages materials so that fracture properties (e.g. ductility and toughness) of the final product may differ from those of the unstrained material. toughness) of the final product may differ from those of the unstrained material. As hardening is often both isotropic and kinematic, prestrain can induce anisotropic hardening properties in addition to the texture related plastic anisotropy [1, 2].

In this study, a X100 grade high strength steel plate is prestrained at different levels. The prestrained material is then tested along different loading directions to investigate both plasticity and damage. A model derived from the Gurson–Tvergaard–Needleman (GTN) model is proposed to represent the behaviour of the material which includes the description of anisotropic plasticity, kinematic hardening and anisotropic ductile damage.

Material and mechanical testing

Material. The material of this study is an experimental X100 grade high strength steel produced in a commercial mill. This class of steel is used to manufacture pipelines. It was supplied as a 16 mm thick plate. The nominal chemical composition is given in Table 1. The plate was elaborated using thermo-mechanical controlled rolling and accelerated cooling (TMCP process). The resulting microstructure is mainly a dual phase structure consisting of fine polygonal ferrite and bainite.

Due to material processing, the plate has an anisotropic plastic behaviour [3] so that it is important to keep track of the material principal axes. In the following the longitudinal direction corresponding to the rolling direction is referred to as L; the transverse direction is referred to as T and the short transverse (thickness) direction is referred to as S. D stands for the diagonal direction (45°) between direction L and T in the sheet plane).

To prestrain the material, large flat tensile specimens (700 mm$\times$150 mm) were machined and strained up to 6% on a 4000 kN tensile machine. The level of prestraining is close to the uniform

elongation of the material; above this limit specimens start to neck. The specimen shape was optimized to produce a 200mm$\times$100mm zone at the center of the specimen where strain is uniform. Strain gauges were glued on the specimen to check the prestrain level. Prestrain is performed along the T direction which corresponds to the prestraining direction during UOE forming of pipes.

C	Si	Mn	P	S	Ti	N
0.051	0.20	1.95	0.007	0.0015	0.012	0.004

Other minor alloying elements: Ni, Cr, Cu, Nb.

Table 1: Nominal chemical composition (weight %).

Mechanical testing. A comprehensive characterisation of the mechanical properties of the material was carried out along the different material directions using several specimen geometries which are depicted in [3]. Prestrain levels were 0%, 2%, 4% and 6%. Levels higher than 6% cannot be reached as this level is close to the necking strain.

Smooth tensile bars were used to determine the hardening behaviour along L, T and D directions. Strain rate equal to $5 \cdot 10^{-4}\text{s}^{-1}$ is kept constant during the test. An extensometer is used to measure elongation. Diameter reduction across the S direction is also measured to obtain the Lankford coefficients. The Lankford coefficient is defined as follows: $R_{\parallel} = \varepsilon_{\perp}/\varepsilon_{\text{S}}$ where $\parallel$ corresponds to the loading direction and $\perp$ to the direction perpendicular to both the loading and S directions. ε corresponds to the true strain. $\varepsilon_{\perp}$ is computed assuming plastic incompressibility.

Axisymmetric notched tensile bars (NT$_\chi$) are used to characterise both plastic behaviour and damage growth. Tests are performed for L and T directions. Different notch radii are used to modify stress state and in particular the stress triaxiality ratio inside the specimens. Radii equal to 0.6, 1.2 and 2.4 mm are used. The axial elongation as well as the minimum diameter variation along the S direction, $\Delta\Phi_{\text{S}}$, are continuously measured. The mean strain rate computed from the diameter variation is controlled and fixed to $5 \cdot 10^{-4}\text{s}^{-1}$.

Wide and relatively thin specimens are used to generate plane strain (PE) conditions (see [3]). Tests were carried out in the L and T directions. Once again the displacement rate was chosen so that the strain rate at the centre of the specimen is about $5 \cdot 10^{-4}\text{s}^{-1}$.

Crack growth resistance was investigated using compact tension (CT) according to the ASTM-1820 standard. Specimens have a total thickness $B = 12.5$ mm and a width $W = 2B = 25$ mm. Specimens were without side grooves. CT specimens were fatigue-precracked to obtain an initial crack length a_0 between $0.55W$ and $0.60W$. The J—Δa resistance curve was determined using the multi-specimen technique in accordance with ASTM-1820. Ductile crack extension was determined from direct measurements of crack advance of specimens which were broken at liquid nitrogen temperature after unloading. To investigate fracture anisotropy two loading configurations were studied: L–T and T–L. For the L–T (resp. T–L) configuration, load is applied in the L (resp. T) direction and crack extends in the T (resp. L) direction.

Plastic behavior

Experimental evidence of plastic anisotropy and mixed isotropic/kinematic hardening. Nominal stress–strain curves obtained for smooth bars tested along the L, D and T directions are shown in Fig. 1 for the as received material and the prestrained materials. Curves are plotted up to the onset of necking. In the as received state, plastic anisotropy is evidenced: flow stresses depend on the loading direction (T being the hardest direction and D the softest). For the prestrain state, necking occurs immediately in the T direction for prestrain levels above 4% indicating that the material lost its hardening capability along this direction. Along L and D directions some hardening capability is retained

for all prestrain levels. This behaviour clearly indicates the occurence of kinematic hardening which was also characterized by performing tension/compression cyclic tests.

In addition, plastic deformation is also anisotropic. As an example, a SEM micrograph of a smooth tensile bar tested along the L direction is shown in Fig. 1 exhiting a much higher deformation along the S direction than along the T-direction. Lankford coefficients measured along the T, L and D directions are respectively equal to 0.67, 0.40 and 1.

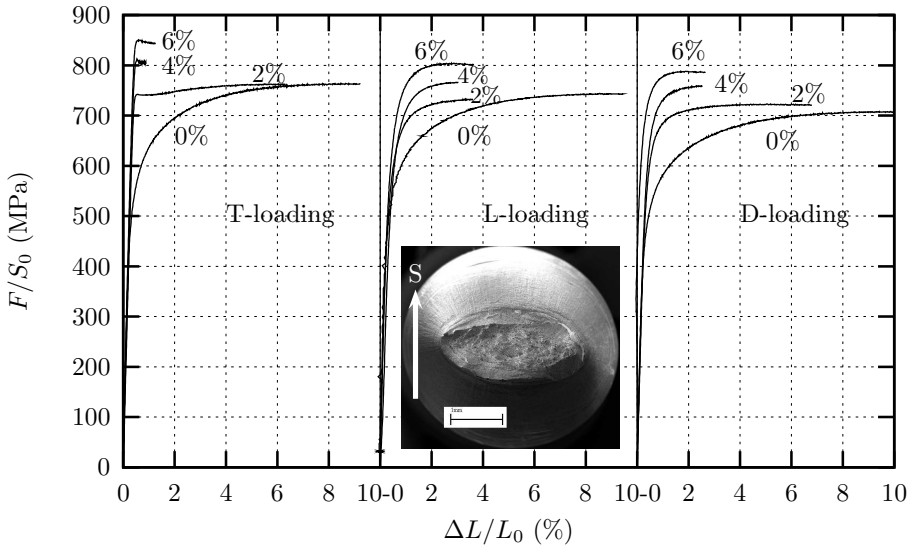

Figure 1: Nominal stress (F/S_0) as a function of strain for T, L and D loading directions for the different prestrain levels.

Model for the plastic behaviour. The model for the plastic behaviour must account for anisotropy and mixed isotropic/kinematic hardening to describe the experimentally found behaviour. Kinematic hardening is represented by an internal back stress tensor $\underline{X}$. The yield surface is then expressed as a function of $\underline{B} = \underline{\sigma} - \underline{X}$, where $\underline{\sigma}$ is the Cauchy stress tensor. Plastic anisotropy is introduced using an anisotropic stress measure B_E defined following the model proposed in [4] and which is a generalization of previously published models [5, 6]:

$$B_E = \left(\sum_{k=1}^{N} \alpha_k B_{Ek}^a \right)^{1/a} \tag{1}$$

with $\sum_k \alpha_k = 1$ and $\alpha_k \geq 0, \forall k$. In the following, two anisotropic scalar stress measures ($N = 2$) are used to define B_E as in [4, 3]. One first defines two modified stress deviators:

$$\underline{B}_k = \underline{\underline{L}}_k : \underline{B} \qquad k = 1, 2 \tag{2}$$

where the fourth order tensor $\underline{\underline{L}}_k$ is expressed as using Voigt notations:

$$\underline{\underline{L}}_k = \begin{pmatrix} \frac{1}{3}(c_{\mathrm{LL}}^k + c_{\mathrm{SS}}^k) & -\frac{1}{3}c_{\mathrm{SS}}^k & -\frac{1}{3}c_{\mathrm{LL}}^k & 0 & 0 & 0 \\ -\frac{1}{3}c_{\mathrm{SS}}^k & \frac{1}{3}(c_{\mathrm{SS}}^k + c_{\mathrm{TT}}^k) & -\frac{1}{3}c_{\mathrm{TT}}^k & 0 & 0 & 0 \\ -\frac{1}{3}c_{\mathrm{LL}}^k & -\frac{1}{3}c_{\mathrm{TT}}^k & \frac{1}{3}(c_{\mathrm{TT}}^k + c_{\mathrm{LL}}^k) & 0 & 0 & 0 \\ 0 & 0 & 0 & c_{\mathrm{TL}}^k & 0 & 0 \\ 0 & 0 & 0 & 0 & c_{\mathrm{LS}}^k & 0 \\ 0 & 0 & 0 & 0 & 0 & c_{\mathrm{ST}}^k \end{pmatrix} \tag{3}$$

The eigenvalues of $\underline{B_k}$ are then computed: $B_k^1 \geq B_k^2 \geq B_k^3$. B_{E1} is then computed as:

$$B_{E1} = \left(\frac{1}{2} \left(|B_1^2 - B_1^3|^{b_1} + |B_1^3 - B_1^1|^{b_1} + |B_1^1 - B_1^2|^{b_1} \right) \right)^{1/b_1} \tag{4}$$

and B_{E2} as:

$$B_{E2} = \left(\frac{3^{b_2}}{2^{b_2} + 2} \left(|B_2^1|^{b_2} + |B_2^2|^{b_2} + |B_2^3|^{b_2} \right) \right)^{1/b_2} \tag{5}$$

Model parameters that need to be adjusted are therefore α_1 ($\alpha_2 = 1 - \alpha_1$), c_i^k ($k = 1, 2$ and $i = \mathrm{TT} \ldots \mathrm{ST}$), a, b_1 and b_2.

The yield function is then defined as:

$$\Phi = B_E - R(p) \tag{6}$$

where p is the effective cumulated plastic strain and $R(p)$ a function representing the size of the elastic domain (isotropic hardening). Plastic flow is then given by the normality rule so that:

$$\underline{\dot{\varepsilon}_p} = \dot{p} \frac{\partial \Phi}{\partial \underline{\sigma}} = \dot{p} \frac{\partial B_E}{\partial \underline{\sigma}} \tag{7}$$

where $\underline{\dot{\varepsilon}_p}$ is the plastic strain rate tensor. p is such that: $\underline{\dot{\varepsilon}_p} : \underline{B} = \dot{p} B_E$. The plastic multiplier $\dot{p}$ is expressed as $\dot{p} = \dot{\varepsilon}_0 (\Phi / \sigma_0)^n$ to account for the slight strain rate dependence of the material. Finally the evolution law for the back stress is given by (non linear kinematic hardening):

$$\underline{\dot{X}} = \frac{2}{3} C \underline{\dot{\varepsilon}_p} - D \dot{p} \underline{X} \tag{8}$$

Model parameters adjustment. The above described model introduces many material parameters which need to be adjusted: $\alpha_{k=1,2}$, a, $b_{k=1,2}$, $c_{k=1,2}^{i=1\ldots6}$, R, C and D. The fit was performed using smooth tensile specimens tested along the different direction for all prestrain levels. Both stress–strain curves and Lankford coefficients were used. In addition, test results on notched bars and plane strain specimens were used. Resulting model parameters are gathered on Table 2.

Ductility and toughness of prestrained materials

Notched bars. Results for notched bars (radius 1.2 mm) are shown in Fig. 2 for the various prestrain levels and for both T and L loading directions. In all cases, load–diameter reduction curves (F/S_0—$\Delta\Phi_S/\Phi_0$) exhibit a sharp load drop which corresponds to the initiation of a macroscopic crack at the center of the specimen. It can also be observed that specimens tested along the L direction show a higher ductility (characterized by the sharp load drop) than specimens tested along the T direction. Finally it is shown that prestrain reduces ductility for prestrain levels between 0 and 4% but that no significant difference is observed for prestrain levels equal to 4 and 6%. Similar conclusions were drawn for the two other notch geometries (0.6 and 2.4 mm).

CT specimens. The J—Δa curves for the as received material are plotted in Fig. 3-a for both L–T and T–L configurations. The material exhibits a higher crack growth resistance when the main loading direction corresponds to the rolling direction. This result is in agreement with results on notched bars (Fig. 2) which exhibit a higher ductility for L loading. Once again rupture anisotropy is evidenced. The same effect is obtained for all prestrain levels.

Fig. 3-b shows the J value corresponding to 1 mm crack advance ($J_{1\mathrm{mm}}$) as a function of prestrain. A sharp drop is observed for prestrain levels between 0 and 4% but $J_{1\mathrm{mm}}$ appears to remain constant

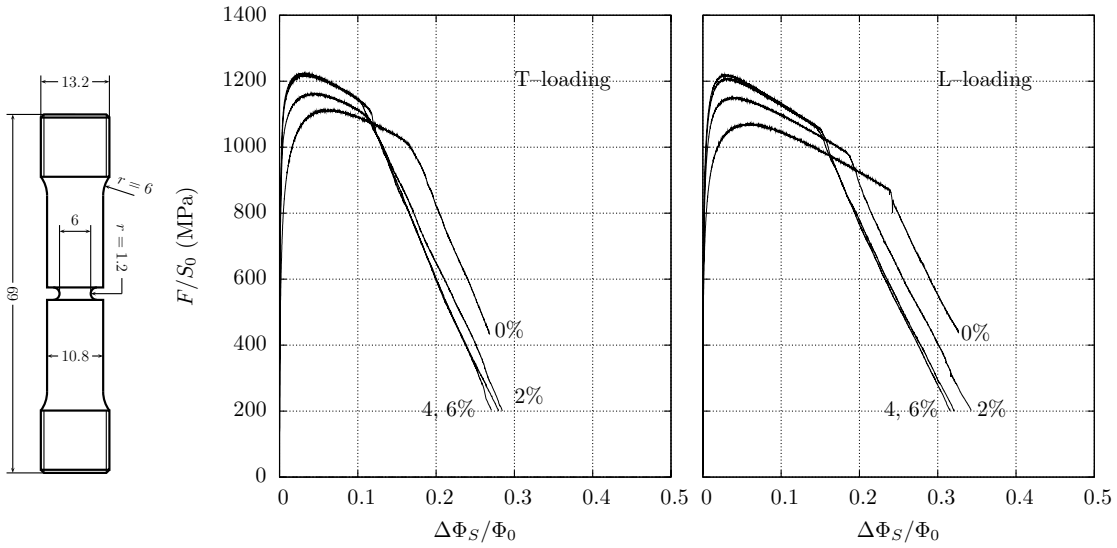

Figure 2: Test results for notched bars ($r = 1.2$ mm) tested along the T and L directions for the various prestrain levels. (F: force, S_0: initial minimal cross-section, Φ_0: initial minimal diameter, $\Delta\Phi_S$: minimal diameter variation along the S direction).

for higher prestrain levels. This trend is in agreement with results on notched bars (Fig. 2) which exhibited similar results for 4% or 6% prestrain.

Failure mechanisms. Fracture surfaces were observed using SEM. Failure is caused by growth and coalescence of primary dimples (about 20 μm) initiated at oxides (mainly TiO_2). For cases where the stress triaxiality ratio is low (i.e. smooth and moderately notched bars) small dimples (about 1 μm) that probably initiated at iron carbides, are also observed. One can assume that large voids are initiated at the early stage of plastic deformation whereas smaller ones require a large amount of plastic deformation to nucleate. The same conclusions were drawn from the study of a similar material [3]. As the prestrain levels remain relatively low compared to failure strains and as prestrain is performed at a low stress triaxiality ($\frac{1}{3}$), it is believed that prestrain does not cause significant damage growth. Consequently, ductility and toughness reductions caused by prestrain are to be related to modification of work hardening capability.

Model for ductile failure

The model for ductile failure must coincide with the model for plastic behavior in absence of damage. In addition, the model must account for rupture anisotropy and primary and secondary void nucleation. The model is based on the Gurson–Tvergaard–Needleman (GTN) model [7, 8] extended to take into account plastic anisotropy and kinematic hardening following [9, 10, 1, 11, 2]. The description of damage anisotropy is based on the simple phenomenological approach proposed in [2]. Damage corresponds to the void volume fraction f. The model is based on the definition of an effective scalar stress measure $a_\star$ expressed as a function of tensor $\underline{a}$ and damage f. It is implicitly defined by solving the following equation:

$$S(\underline{a}, f, a_\star) = \frac{a_E^2}{a_\star^2} + 2q_1 f_\star \cosh\left(\frac{q_2}{2}\frac{a_K}{a_\star}\right) - 1 - q_1^2 f_\star^2 \equiv 0 \qquad (9) \quad \texttt{\{eq:S\}}$$

$f_\star$ is a function of damage introduced to model final failure by coalescence [7]. q_1 and q_2 are model parameters. The anisotropic stress measure a_E is used to account for plastic anisotropy [1]. a_K is used

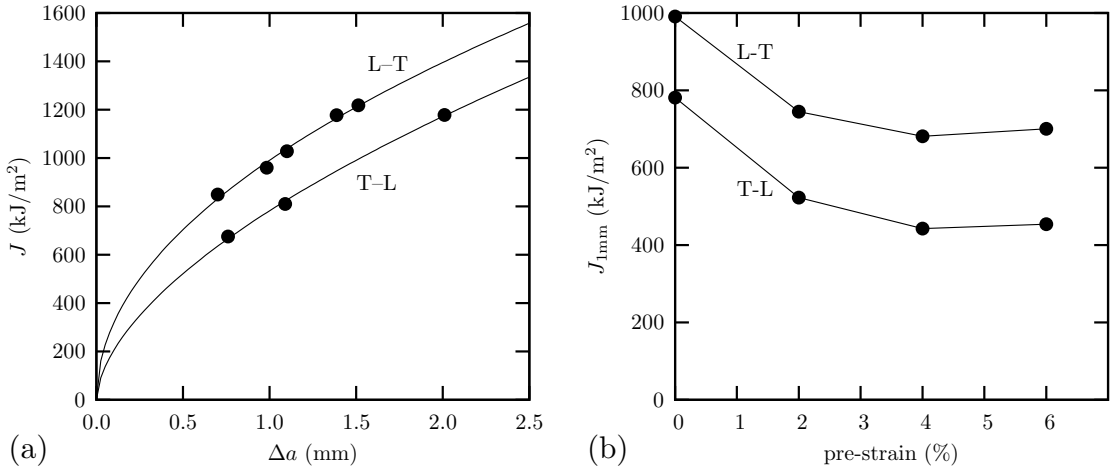

Figure 3: (a) J—Δa curves for T–L and L–T configurations for the as received material. (b) $J_{1\mathrm{mm}}$ for T–L and L–T configurations as a function of prestrain.

to account for anisotropic ductile damage instead of the trace of $\underline{a}$ as in the original GTN model [2]. It is expressed as:

$$a_K = \alpha_{\mathrm{LL}} a_{\mathrm{LL}} + \alpha_{\mathrm{TT}} a_{\mathrm{TT}} + \alpha_{\mathrm{SS}} a_{\mathrm{SS}} \tag{10}$$

The yield function is then expressed as:

$$\Phi = B_\star - R(p) \tag{11}$$

where $B_\star$ is defined by $S(\underline{B}, f, B_\star) = 0$. Using the normality rule, the plastic strain rate tensor is given by:

$$\underline{\dot{\varepsilon}}_p = (1-f)\frac{\partial \Phi}{\partial \underline{\sigma}} = (1-f)\frac{\partial B_E}{\partial \underline{\sigma}} \tag{12}$$

One has: $\underline{\dot{\varepsilon}}_p : \underline{B} = (1-f)\dot{p}B_E$. Damage growth is described considering void growth and void nucleation on carbides so that:

$$\dot{f} = (1-f)\mathrm{trace}\underline{\dot{\varepsilon}}_p + A_n \dot{p} \tag{13}$$

where A_n is the nucleation rate. Primary particles are assumed to debond/break at the onset of plastic strain so that the initial void volume fraction f_0 corresponds the particles volume fraction. The back stress $\underline{X}$ is defined using an intermediate stress $\underline{\chi}$ defined by the following equation [9, 11]:

$$\underline{\dot{\chi}} = \frac{2}{3} C \underline{\dot{\varepsilon}}_p - D\dot{p}\underline{\chi} \tag{14}$$

$\underline{X}$ is then such that:

$$\underline{\chi} = \frac{2}{3} X_\star^{\mathrm{iso}} \frac{\partial X_\star^{\mathrm{iso}}}{\partial \underline{X}} \tag{15}$$

where $X_\star^{\mathrm{iso}}$ is computed using eq. 9 using the von Mises and trace invariants of $\underline{X}$ instead of the anisotropic measures. A preliminary fit of the different model parameters was performed. Model parameters are gathered in Table 2.

Simulation of prestrain effects

Details of the finite element (FE) simulation techniques can be found in [1]. Quadratic elements with reduced integration were used. Simulations for notched bars are shown in Fig. 4 for both T

Elastic properties	Young's modulus: 200 GPa, Poisson's ratio: 0.3
Plastic hardening	$R(p) = 375(1 + 0.15(1 - \exp(-78p)) + 0.52(1 - \exp(-14p)))$ (MPa)
Kinematic hardening	$C = 39800$ (MPa), $D = 287$
Plastic anisotropy	$a = b_1 = b_2 = 8.8$, $\alpha_1 = 0.70$, $\alpha_2 = 0.30$
	$c^1_{\mathrm{TT}} = 1.05$, $c^1_{\mathrm{LL}} = 0.82$, $c^1_{\mathrm{SS}} = 0.66$, $c^1_{\mathrm{TL}} = 0.93$, $c^1_{\mathrm{LS}} = 1.16$, $c^1_{\mathrm{ST}} = 1.20$
	$c^2_{\mathrm{TT}} = 0.94$, $c^2_{\mathrm{LL}} = 1.05$, $c^2_{\mathrm{SS}} = 0.75$, $c^2_{\mathrm{TL}} = 0.80$, $c^2_{\mathrm{LS}} = 0.99$, $c^2_{\mathrm{ST}} = 1.22$
Initial porosity	$f_0 = 5.8 \cdot 10^{-4}$
GTN model	$q_1 = 1.39$, $q_2 = 1.$, $f_\star = \begin{cases} f & \text{if } f < 0.05 \\ 0.05 + 4.5(f - 0.05) & \text{otherwise} \end{cases}$
Rupture anisotropy	$\alpha_{\mathrm{TT}} = 1.18$, $\alpha_{\mathrm{LL}} = 0.73$, $\alpha_{\mathrm{SS}} = 1.21$
Carbide nucleation	$A_n = \begin{cases} 0 & \text{if } p < 0.8 \\ 0.5 & \text{otherwise} \end{cases}$

Table 2: Material model parameters

and L loading directions for all prestrain levels. Experimental trends (Fig. 2) are well reproduced: anisotropic ductility and ductility reduction by prestrain. Simulations of the J—Δa curves for the as received state are shown in Fig. 5. J and Δa were computed from the simulation according to the ASTM–1820 standard. Ductile tearing anisotropy is well reproduced. Simulations of the J—Δa curves for the various prestrain levels in the T–L configuration are shown in Fig. 6 together with the Load–crack mouth opening displacement (CMOD) curves. As experimentally observed crack growth resistance decreases with increasing prestrain level. It is interesting to note that prestraining leads to an increase of the maximum force but that load decrease is faster. This last trend was also experimentally observed.

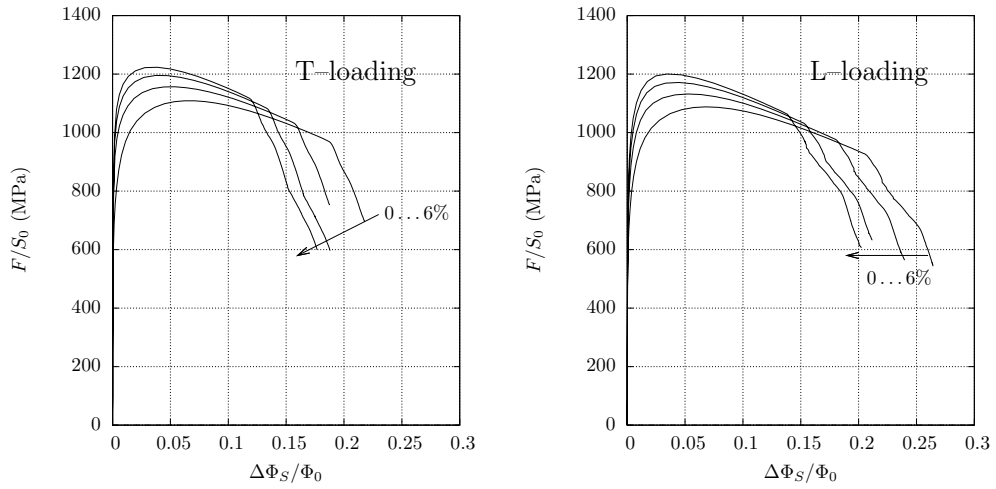

Figure 4: FE simulation for notched bars (notch radius: 1.2 mm) for T and L loading directions for all prestrain levels.

References

[1] Bron, F. and Besson, J. (2006) *Eng. Fract. Mech.*, **73**, 1531–1552.

[2] Morgeneyer, T.M. and Besson, J. and Proudhon, H. and Starink, M.J. and Sinclair, I. (2009) *Acta Mater.*, **57** (13), 3902–3915.

[3] Tanguy, B. and Luu, T.T. and Perrin, G. and Pineau, A. and Besson, J. (2008) *Int. J. of Pressure Vessels and Piping*, **85** (5), 322–335.

[4] Bron, F. and Besson, J. (2004) *Int. J. Plasticity*, **20**, 937–963.

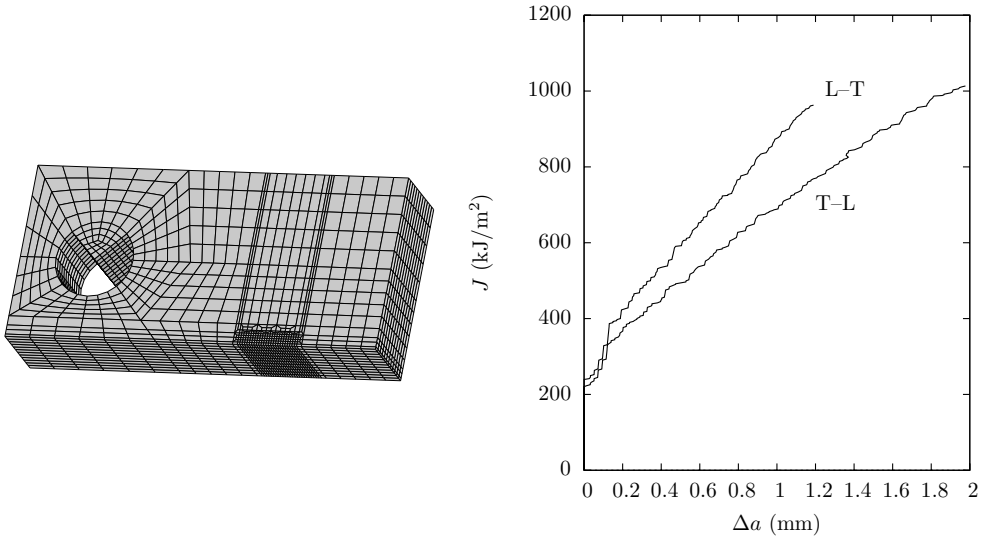

Figure 5: FE simulation of CT tests carried out in the T–L and L–T configurations. A FE mesh is also shown.

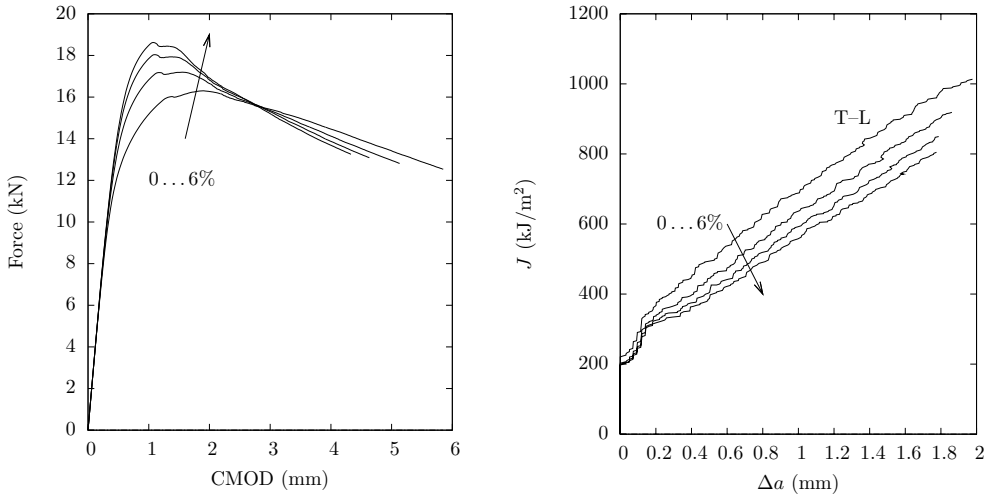

Figure 6: FE simulation of CT tests carried out in the T–L configuration for various prestrain levels. Load–CMOD curves and J—Δa curves.

[5] Karafillis, A.P. and Boyce, M.C. (1993) *J. Mech. Phys. Solids*, **41**, 1859–1886.

[6] Barlat, F. and Lege, D.J. and Brem, J.C. (1991) *Int. J. Plasticity*, **7**, 693–712.

[7] Tvergaard, V. (1990) *Advances in Applied Mechanics*, **27**, 83–151.

[8] Besson, J. (2010) *Int. J. Damage Mech.*, **19**, 3–52.

[9] Besson, J. and Guillemer–Neel, C. (2003) *Mechanics of Materials*, **35**, 1–18.

[10] Rivalin, F. and Besson, J. and Di Fant, M. and Pineau, A. (2000) *Eng. Fract. Mech.*, **68** (3), 347–364.

[11] Besson, J. (2009) *Int. J. Plasticity*, **25**, 2204–2221.